

Ultrathin PdAuBiTe Nanosheets as High-Performance Oxygen Reduction Catalysts for a Direct Methanol Fuel Cell Device

Fengling Zhao, Lirong Zheng, Qiang Yuan,* Xiaotong Yang, Qinghua Zhang, Han Xu, Yuanlong Guo, Song Yang,* Zhiyou Zhou,* Lin Gu,* and Xun Wang*

Ultrathin 2D metal nanostructures have sparked a lot of research interest because of their improved electrocatalytic properties for fuel cells. So far, no effective technique for preparing ultrathin 2D Pd-based metal nanostructures with more than three compositions has been published. Herein, a new visible-light-induced template technique for producing PdAuBiTe alloyed 2D ultrathin nanosheets is developed. The mass activity of the PdAuBiTe nanosheets against the oxygen reduction reaction (ORR) is $2.48 \text{ A mg}_{\text{Pd}}^{-1}$, which is 27.5/17.7 times that of industrial Pd/C/Pt/C, respectively. After 10 000 potential cyclings, there is no decrease in ORR activity. The PdAuBiTe nanosheets exhibit high methanol tolerance and in situ anti-CO poisoning properties. The PdAuBiTe nanosheets, as cathode electrocatalysts in direct methanol fuel cells, can thus give significant improvement in terms of power density and durability. In O_2/air , the power density can be increased to $235.7/173.5 \text{ mW cm}^{-2}$, higher than that reported in previous work, and which is 2.32/3.59 times higher than Pt/C.

conditions at 25°C , while that of proton exchange membrane fuel cells is 0.83. Due to sluggish kinetics, poor methanol tolerance, and susceptibility to CO poisoning for the state-of-the-art Platinum (Pt) electrocatalyst at the cathode side, the oxygen reduction reaction (ORR) is the main process in practical DMFCs, delaying the commercialization of DMFCs significantly. Therefore, significant research efforts are being focused on the development of high-performance alternatives to Pt materials. Among the various potential ORR electrocatalysts, Palladium (Pd)-based electrocatalysts are the most promising substitutes for Pt in alkaline electrolytes.^[1–4]

It is believed that the surface composition, size, and shape of the electrocatalysts seriously affect their ORR performances because of surface atomic arrangement, defect, electronic effect, and


surface strain.^[5–10] In a variety of nanostructures, the ultrathin 2D nanostructures have received extensive attention due to their intrinsic advantages, such as high surface metal atom to volume ratio and abundant low-coordinated atoms (e.g., top-most surface atoms and edge atoms).^[11–15] Moreover, lattice strains, geometric effects, and ensemble effects present in multimetallic catalysts often boost the ORR activities.^[16–21] Due to

1. Introduction

Since methanol is readily available and stored, as well as having a high energy density, direct methanol fuel cells (DMFCs) are promising for renewable clean energy conversion devices to mitigate the energy crisis and greenhouse effect. Besides, the reversible energy efficiency of DMFCs is 0.967 under ambient

F. Zhao, Prof. Q. Yuan, X. Yang, Prof. S. Yang
State-Local Joint Laboratory for Comprehensive Utilization of Biomass
Center for R&D of Fine Chemicals
College of Chemistry and Chemical Engineering
Guizhou University
Guiyang, Guizhou Province 550025, P. R. China
E-mail: qyuan@gzu.edu.cn; yangsdqj@126.com
Dr. L. Zheng
Beijing Synchrotron Radiation Facility Institute of High Energy Physics
Chinese Academy of Sciences
Beijing 100049, P. R. China
Prof. Q. Yuan, Prof. X. Wang
Key Lab of Organic Optoelectronics & Molecular Engineering
Tsinghua University
Beijing 100084, P. R. China
E-mail: wangxun@mail.tsinghua.edu.cn

Q. Zhang, H. Xu, Prof. L. Gu
Chinese Academy of Sciences and Beijing National Laboratory
for Condensed Matter Physics
Beijing 100190, P. R. China
E-mail: l.gu@iphy.ac.cn
Y. Guo
College of Materials and Metallurgy
Guizhou University
Guiyang, Guizhou Province 550025, P. R. China
Prof. Z. Zhou
State Key Laboratory of Physical Chemistry of Solid Surfaces
College of Chemistry and Chemical Engineering
Xiamen University
Xiamen 361005, P. R. China
E-mail: zhouzy@xmu.edu.cn

 The ORCID identification number(s) for the author(s) of this article can be found under <https://doi.org/10.1002/adma.202103383>.

DOI: 10.1002/adma.202103383

the thermodynamically disadvantageous for the growth of 2D ultrathin nanostructures and the intrinsic physical and chemical properties of the parent metals, such as crystal phase, lattice mismatch, and redox potential, the synthesis of multi-metallic 2D nanostructures has become a priority and challenging problem in synthetic nanochemistry in order to incorporate these properties into 2D nanostructures. To date, successful progress in the synthesis of ultrathin 2D metal nanostructures mainly focused on monometallic, binary metals, and limited ternary metals,^[22–29] and to the best of our knowledge, no 2D quaternary Pd-based metal nanostructure has been reported.

The overall ORR in alkaline medium is $\text{O}_2 + 2\text{H}_2\text{O} + 4\text{e}^- \rightarrow 4\text{OH}^-$, in which H_2O is the proton donor and includes the surface intermediate species, such as HOO^* , O^* , and HO^* .^[30–32] Therefore, in addition to the activation and fracture of $\text{O}-\text{O}$ band, the activation of water as well as appropriate adsorption and desorption of HO^* intermediates that are the final intermediates from O_2 to OH^- (Namely, $\text{HO}^* + \text{e}^- \rightarrow \text{OH}^-$), are also key intermediate processes for enhancing ORR activity.^[33–36] While Pd alloying with transitional metals can change surface reactivity due to ensemble effects, lattice strain, and ligand impact, which facilitates the activation of O_2 and H_2O while weakening the adsorption strength of oxygen-containing intermediates, result in improved ORR.^[37–44] Adzic et al. reported that $\text{Au}_{10}\text{Pd}_{40}\text{Co}_{50}$ electrocatalyst displayed superior ORR activity and durability after 10 000 potential cyclings to commercial Pt/C.^[43] Recently, Huang et al. reported that $\text{Pd}_{20}\text{Te}_7$ hexagonal nanoplates demonstrated an ORR mass activity (MA) of $(0.30 \text{ A mg}_{\text{Pd}}^{-1})$ at 0.90 V versus reversible hydrogen electrode (RHE) and a maximal power density of 109 mW cm^{-2} in practical DMFCs.^[28] Although high-performance ORR electrocatalysis has been reported, there are rare reports on their applications for practical DMFCs, mainly concentrated at the glassy carbon electrode level. Therefore, for practical DMFC applications, it is highly desirable to find a high-performance ORR electrocatalyst to boost the power density and durability of DMFCs.

In this work, we first report a surfactant and reducing agent-free, visible-light-induced method for the preparation of ultrathin 2D quaternary PdAuBiTe, ternary PdBiTe, and AuBiTe alloyed nanosheets (ANSs) with a thickness of $\approx 5 \text{ nm}$ by using ultrathin 2D Bi_2Te_3 nanosheets (Figure S1, Supporting Information) as templates. The PdAuBiTe ANSs exhibit much higher ORR MA and longer durability than 2D ternary PdBiTe ANSs, commercial Pt/C and Pd/C. Simultaneously, the PdAuBiTe ANSs demonstrate high methanol tolerance and antipointing to CO. When coupling the optimized PdAuBiTe ANSs with commercial Pt/C, the power density of DMFC boosts up to 235.7 and 173.5 mW cm^{-2} in O_2 and air, respectively, which are the highest reported values so far. After 54 000 s of durability test fixed at 200 mA cm^{-2} in O_2 , the cell voltage of PdAuBiTe ANSs and Pt/C couples was found to decay by only 15.0%, while the Pt/C couples decayed by 55.1%. And in the air atmosphere, it also showed good durability in 72 000 s of testing.

2. Results and Discussion

The scanning electron microscopy (SEM) images (Figure 1a) demonstrate the as-prepared products consist of 2D irregular

nanosheets. The energy-dispersive X-ray (EDX) spectra confirmed the presence of Pd, Au, Bi, and Te elements. The atomic rates of Pd:Au:Bi:Te determined by the inductively coupled plasma optical emission spectrometry (ICP-OES) was found to be 578:19.9:78:14.5 (marked as PdAuBiTe). The 2D nanosheet-shape structure was further examined by atomic force microscopy (AFM) (Figure 1b–g), and the thickness of the 2D nanosheet is about 5 nm (Figure 1d,g). The surface and side edges of 2D nanosheets are somewhat rough, which could be of advantage concerning surface areas and edge defects. The aberration-corrected high-resolution transmission electron microscopy (HRTEM) images (Figure 2a,b; Figure S2, Supporting Information) further revealed the roughness of the surface and the side edge of PdAuBiTe ANSs. Some nanopores are observed in the nanosheets, which can add low-coordinated edge atoms. The fast Fourier transform (FFT) images (Figure 2a, inset) show that the PdAuBiTe ANSs belong to a face-centered cubic phase terminated by (111) facets and the lattice spacing is 0.228 nm (Figure 2c), which is closed to that of the Pd (111) facet. Furthermore, defects such as lattice distortion and atomic dislocation are also observed in the HRTEM images (Figure 2d–f), which could induce local lattice strains.^[42,45] Energy-dispersive X-ray (EDX) element mappings (Figure S3, Supporting Information) show that the Pd, Au, Bi, and Te are uniformly distributed in the nanosheet and the Pd atoms are surrounded by neighboring Au, Bi, and Te atoms, which reveals by atomic HRTEM images (Figure 2g,h) and manifests the formation of Pd–Au, Pd–Bi, and Pd–Te bonds. The coordination environment of the Pd atoms was modified by the vicinity of the dissimilar metal atoms, thereby producing an electronic effect and constructing a dual active site, finally affecting the d-band center of the Pd atoms and modulating the surface reactivity of 2D nanosheets.^[27,28,46–50]

Powder X-ray diffraction (XRD) patterns (Figure 3a; Table S1, Supporting Information) of the PdAuBiTe ANSs demonstrate an (111) diffraction peak relative to other peaks, which resembles that of PdBiTe ANSs (Figures S4–S7, Supporting Information), indicating that the PdAuBiTe ANSs is terminated by (111) facets. The diffraction peaks of the PdAuBiTe ANSs show a negative shift compared to the standard diffraction peaks of Pd (PDF#46-1043), indicating the alloyed nature of the PdAuBiTe ANSs. The negative shift of the diffraction peak is caused by lattice contraction, resulting in a compressive strain and subsequently favoring the ORR activity.^[38–44] The X-ray photoelectron spectra (XPS) (Figure 3b) demonstrate that the Pd mainly shows a metallic state (Pd^0) with a small amount of oxidation state (Pd^{2+}), which is similar to the near-surface Pd state of 2D PdBiTe ANSs (Figures S4–S7, Supporting Information). The binding energy (BE) of Pd in PdAuBiTe ANSs shows a negative shift of about 0.23 eV relative to commercial Pd black. It is worthy to note that the BE of Pd in PdBiTe ANSs show positive shift relative to commercial Pd black, which means that the introduction of Au can reduce the BE of Pd and the downshift of the d-band center of Pd.^[43,48,49] This was further confirmed by the valence band spectra of Pd (Figure 3c). The d-band center of Pd in PdAuBiTe ANSs is -3.42 eV that downshifts relative to that in commercial Pd black (-3.16 eV) and PdBiTe ANSs (-3.06 eV). The Au 4f (Figure 3d) and Te 3d (Figure 3e) spectra show that Au and Te elements are in metallic states in the near-surface

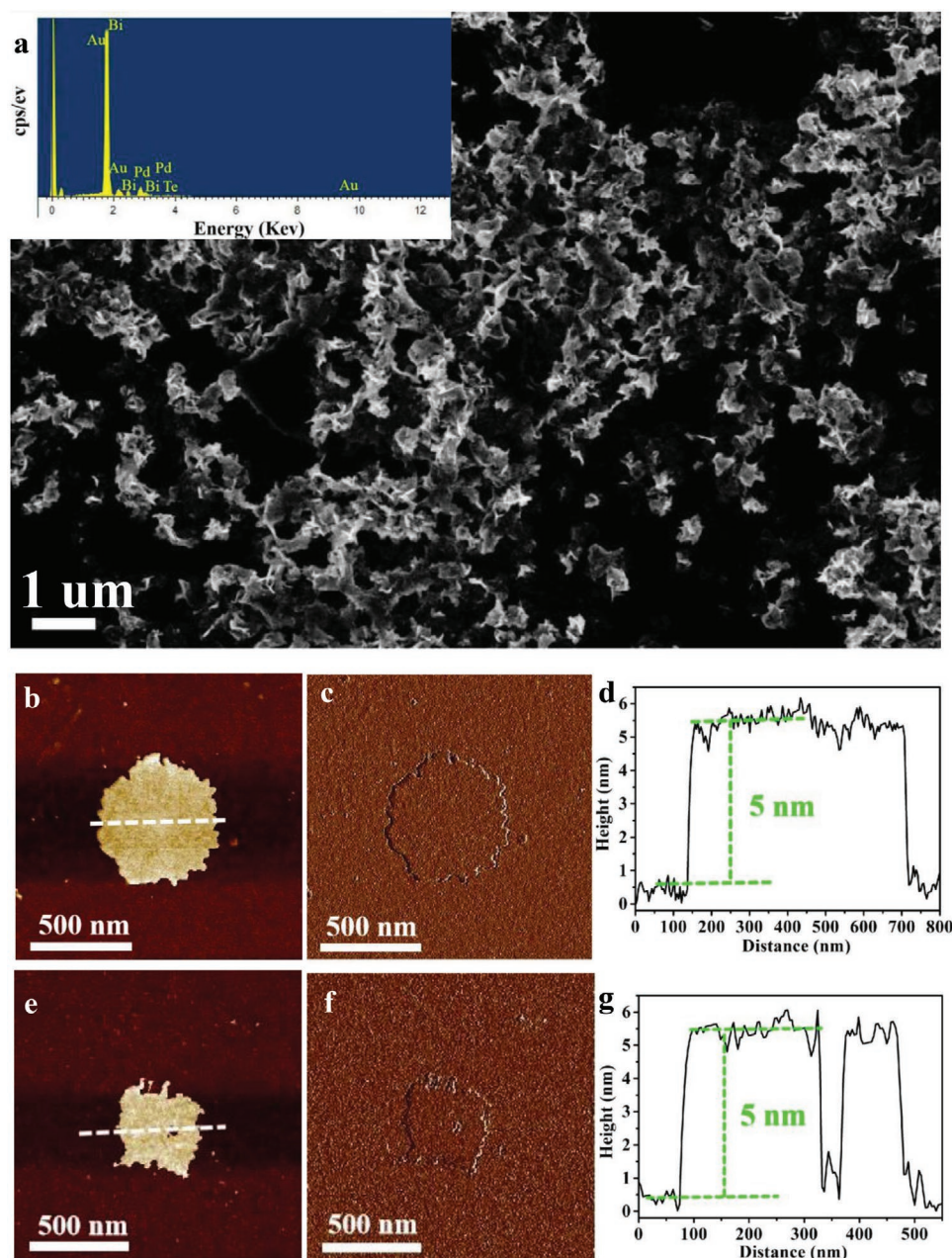


Figure 1. Morphology characterization of PdAuBiTe ANSs. a) SEM (the inset is the EDX spectra). b–g) AFM images and the corresponding height profiles of PdAuBiTe ANSs.

of PdAuBiTe ANSs. The Bi 4f (Figure 3f) spectra show the Bi element coexists in both metallic (Bi^0) and oxidation (Bi^{3+}) states in the near-surface of PdAuBiTe ANSs. The near-surface Au, Bi, and Te have been shown to improve surface reactivity of the alloyed nanocrystals, thereby enhancing the ORR activity.^[6,28,40,41,51] Furthermore, the results of the extended X-ray absorption fine structure (EXAFS) analysis on PdAuBiTe ANSs reveals that the Au is in a metallic state (Au^0) (Figure 4a). There are two kinds of metallic bonds concerning Au, namely the Au–Pd and Au–Au bonds (Figure 4b; Figure S8 and Table S2, Supporting Information), in PdAuBiTe ANSs, which is further confirmed by Au L_3 -edge EXAFS analysis (Figure 4c) and the

corresponding wavelet transform plots (Figure 4d) of PdAuBiTe ANSs. The coordination numbers for Au–Pd and Au–Au are 2.4 and 6.4, respectively, suggesting that Au exists in a low coordination state in the near-surface of PdAuBiTe ANSs, since the coordination number for bulk Au with *fcc* structure is 12. Previous studies confirmed that the low-coordinated Au or Au–Pd dual sites would enhance the ORR performance.^[9,41,43,52–56]

The ORR performances of the as-prepared 2D alloyed PdAuBiTe ANSs were evaluated in KOH solution, and as a reference, the performances of Bi_2Te_3 nanosheets, AuBiTe ANSs (Figures S9 and S10, Supporting Information), PdBiTe ANSs, commercial Pd/C, and Pt/C were also tested. The

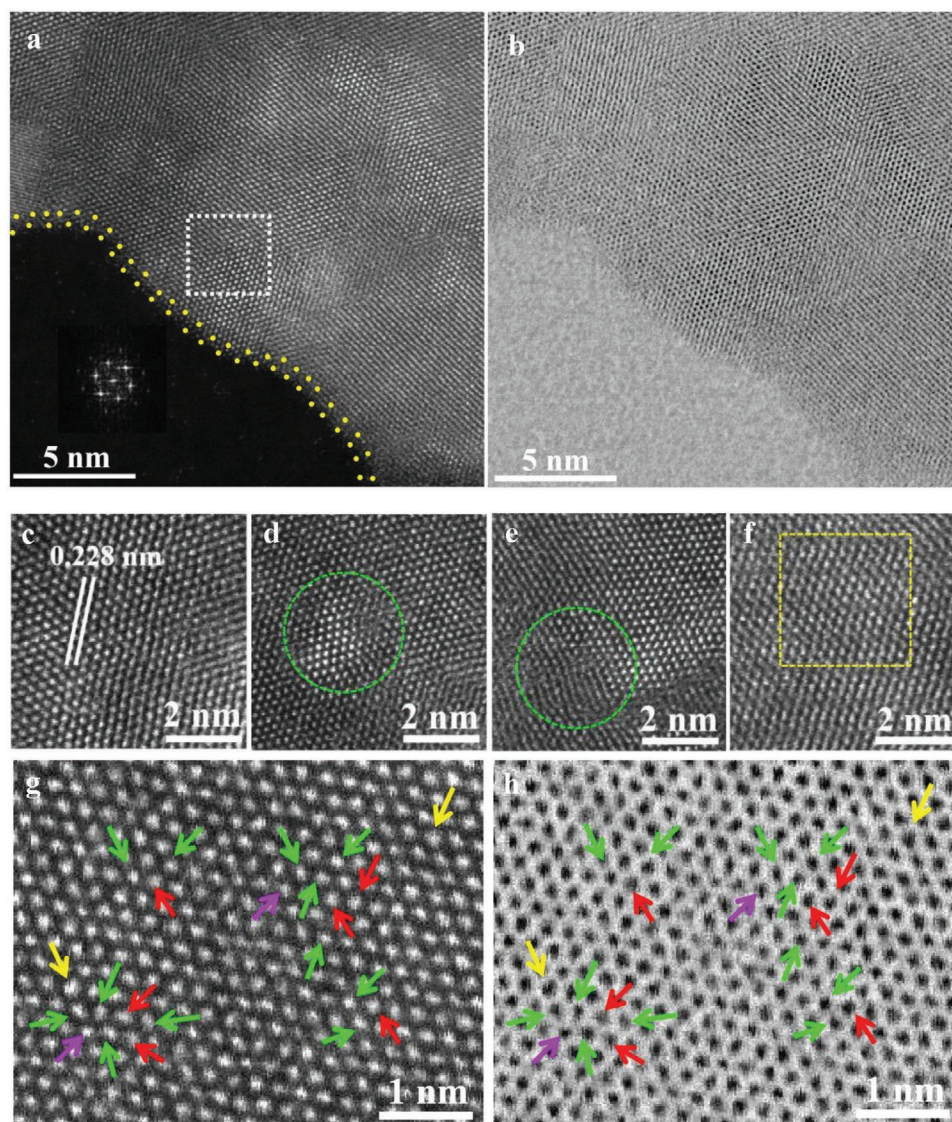


Figure 2. Surface structure characterization of PdAuBiTe ANSs. a–c) The aberration-corrected high-resolution transmission electron microscopy (HRTEM) images: a) in dark field (edge atom in yellow dots; the inset in (a) is the corresponding FFT patterns of the dashed white rectangle), b) in bright field, c) the lattice spacing of PdAuBiTe. d,e) Lattice distortion (in the green dashed circle). f) Atomic dislocation (in the yellow dashed rectangle). g) (In dark field) and h) (in bright field) atomic HRTEM images (atoms are represented by the arrows of different colors—green: Pd, red: Au, yellow: Bi, purple: Te. Atomic radius: Bi > Au > Te = Pd).

electrochemically active surface area (ECSA) of the Pd-based samples and Pt/C were obtained by cyclic voltammetry (CV) (Figure S11a,b, Supporting Information) recorded in N₂-saturated 0.1 M KOH solution. The ECSA values of the PdAuBiTe, PdBiTe, Pd/C, and Pt/C were 63.1, 57.5, 47.4 m² g_{Pd}^{−1}, and 63.6 m² g_{Pt}^{−1}, respectively. The ORR polarization curves (Figure 5a) show the half-wave potential ($E_{1/2}$) and ORR onset potential of PdAuBiTe is 0.929/0.989 V, which is more positive than that of PdBiTe (0.897/0.968 V), Pd/C (0.839/0.937V), and Pt/C (0.851/0.943 V), implying much higher ORR activity on the PdAuBiTe ANSs. The slope of Tafel plots (Figure 5b) of the PdAuBiTe ANSs is 54.9 mV dec^{−1} which is much smaller than that of Pd/C (74.6 mV dec^{−1}), Pt/C (72.3 mV dec^{−1}), and PdBiTe (61.1 mV dec^{−1}) samples, suggesting enhanced ORR kinetics on the PdAuBiTe ANSs. The specific activity (SA)/mass activity (MA)

at 0.9 V versus reversible hydrogen electrode (RHE) (Figure 5c) of PdAuBiTe, PdBiTe, Pd/C, and Pt/C is 3.93 mA cm^{−2}/2.48 A mg_{Pd}^{−1}, 1.27 mA cm^{−2}/0.73 A mg_{Pd}^{−1}, 0.19 mA cm^{−2}/0.09 A mg_{Pd}^{−1}, and 0.22 mA cm^{−2}/0.14 A mg_{Pt}^{−1}, respectively. The MA of PdAuBiTe is 27.5, 17.7, and is 3.4 times that of Pd/C, Pt/C, and PdBiTe ANSs. The introduction of Au into the PdBiTe ANSs was found to be crucial for significantly enhancing the ORR activity due to the low coordinated Au and Au–Pd dual sites in the near-surface. This conclusion was further supported by the higher ORR activity of AuBiTe nanoalloys than that of Bi₂Te₃ nanosheets (Figure S11c, Supporting Information). Moreover, the polarization curves (Figure S11d, Supporting Information) recorded from 400 to 2500 rpm and Koutecky–Levich plots (Figure S11e, Supporting Information) indicate that the ORR process on PdAuBiTe ANSs is via a 4-electron pathway.

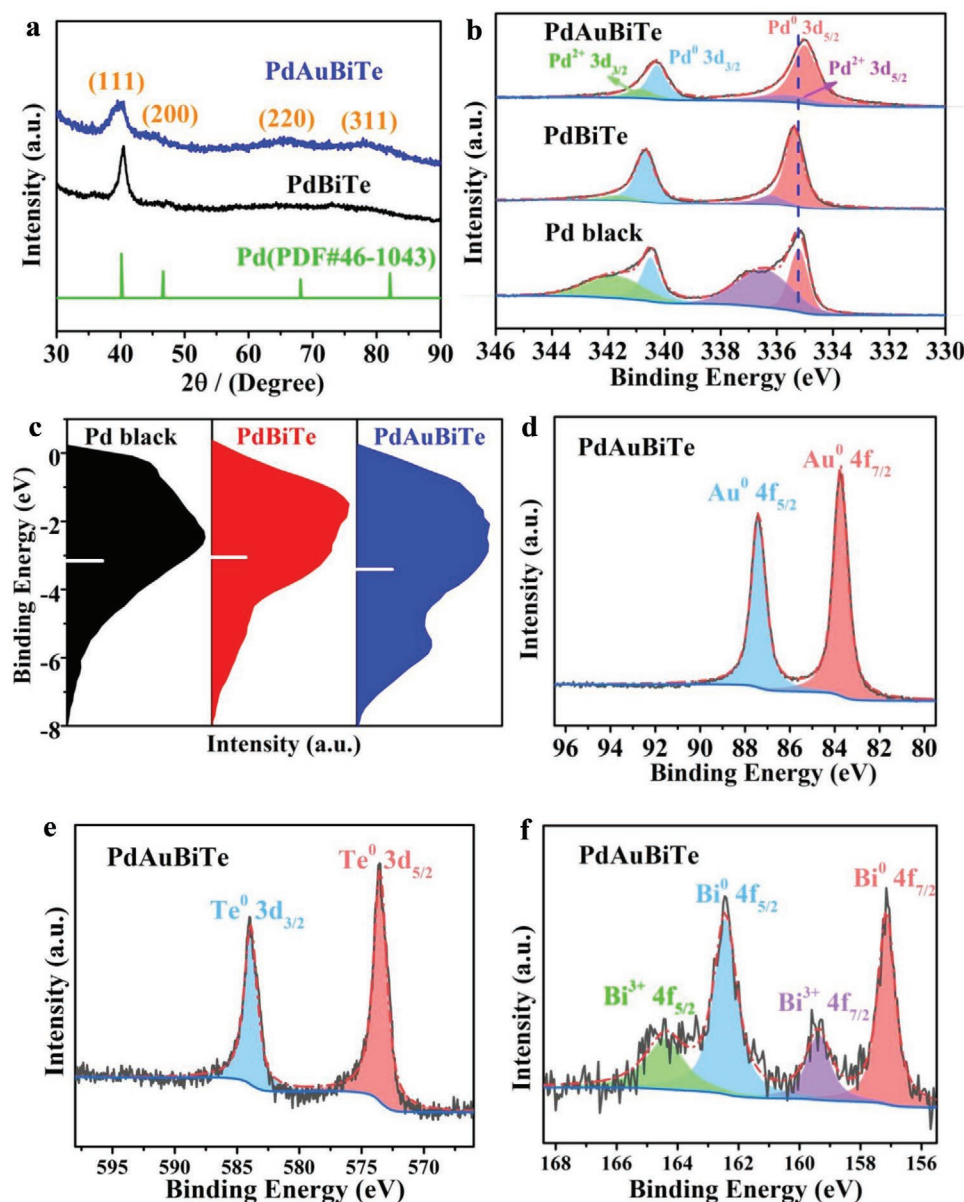


Figure 3. Structure and surface element analysis of PdAuBiTe ANSs. a) XRD spectra of PdBiTe and PdAuBiTe. b,c) XPS spectra of Pd black, PdBiTe, and PdAuBiTe: b) Pd 3d region, and c) surface valence bands. d) Au 4f region, e) Te 3d region, f) Bi 4f region.

Accelerated durability test (ADT) (Figure 5d) shows, after 10 000 potential cycles, for PdAuBiTe ANSs, that the LSV curve almost overlaps the initial one; however, for PdBiTe ANSs, commercial Pt/C, and Pd/C, the LSV curves shift toward negative compared with the initial ones, and the value of half-wave potential correspondingly decreased by 12, 25, and 18 mV. This demonstrates that the PdAuBiTe ANSs has superior durability to PdBiTe ANSs, industrial Pd/C, and Pt/C and reflects that the introduction of Au can improve durability further. Since the methanol or CO formed by methanol oxidation at the anode side will diffuse through the polymer electrolyte membrane to the cathode side and poison the cathode electrocatalyst, significantly degrade electrochemical efficiency, methanol tolerance, and resistance to CO toxicity of the cathodic catalyst are

the key parameters for practical DMFC applications. As shown in Figure 5e and Figure S12, Supporting Information, under the ORR conditions, although the methanol oxidation peaks appeared around 0.83 V on PdAuBiTe ANSs, the half-wave potential ($E_{1/2}$) barely moved. The $E_{1/2}$ on PdBiTe shifted toward negative by 11 mV (Figure S12a, Supporting Information). However, the $E_{1/2}$ negative movement on Pd/C (Figure S12b, Supporting Information) and Pt/C (Figure S12c, Supporting Information) shows that the PdAuBiTe ANSs has enhanced methanol tolerance. In situ CO poisoning tests were performed by injecting CO during the ORR process, which reflect the resistance of the cathode catalyst to CO than the CO-stripping measurement. Figure 5f shows that the platform of the ORR polarization curve shifted upward after injecting CO, which

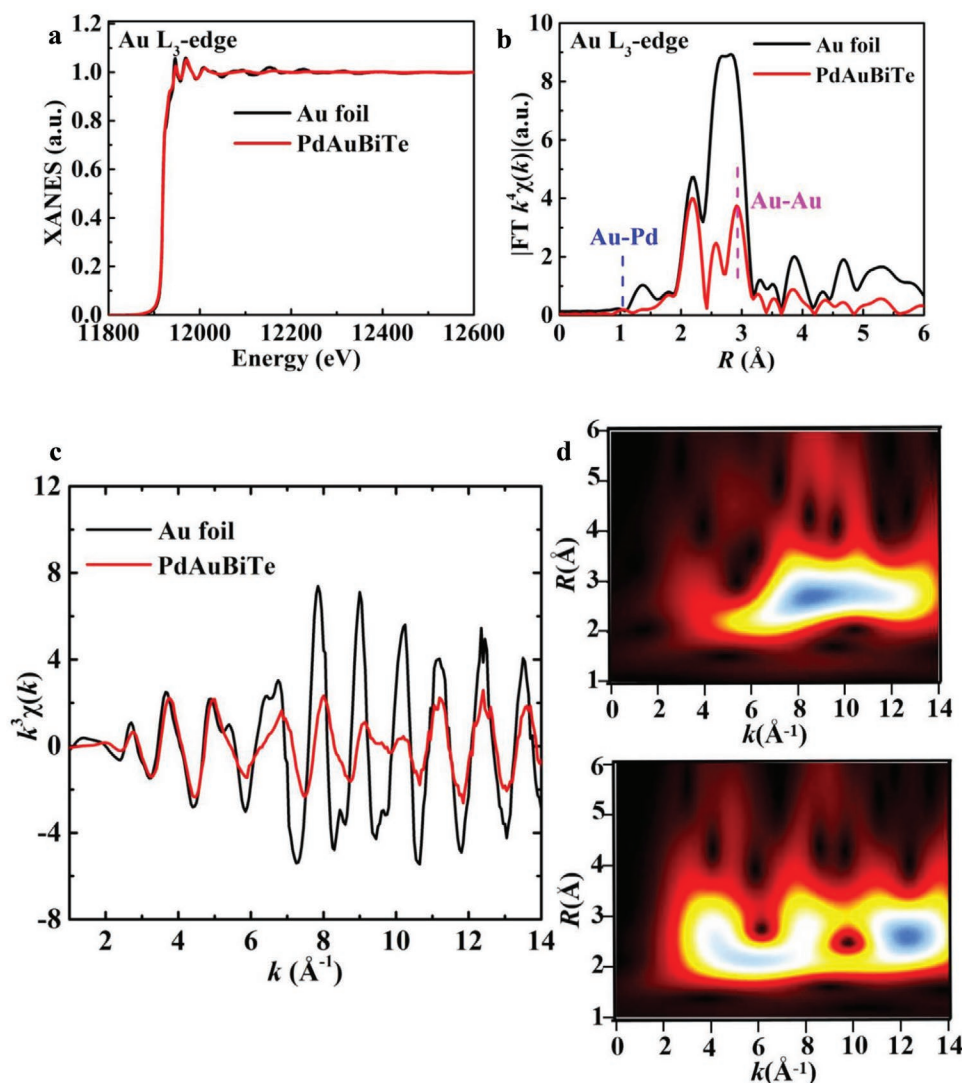


Figure 4. Results of the EXAFS spectroscopy of PdAuBiTe ANSs. a) Normalized Au L₃-edge X-ray absorption near-edge structure (XANES) spectra, b) Fourier transformed spectra, c) k^3 -weighted Au L₃-edge k -space oscillations of Au foil and PdAuBiTe. d) Wavelet transform plots of Au foil (top) and PdAuBiTe (bottom).

could be attributed to CO adsorption occupying some active sites, resulting in oxygen desaturation on the surface of electrocatalysts. CO poisoning occurred on the Pd/C catalyst. Before 0.7 V, a wide CO oxidation peak was observed on PdAuBiTe ANSs, PdBiTe ANSs, and Pt/C, the $E_{1/2}$ of PdAuBiTe showed a negative shift by 6 mV that is less than that of PdBiTe (7 mV), Pt/C (12 mV), and Pd/C (44 mV), indicating that PdAuBiTe and PdBiTe ANSs have much higher resistance to CO poisoning than monometallic Pd or Pt electrocatalyst. This was further demonstrated by increasing the flow rate of CO (Figure S13, Supporting Information). The superior electrochemical performances of the PdAuBiTe ANSs have encouraged us to test its potential applications in practical DMFCs.

The practical DMFC performances of a single cell assembled with PdAuBiTe or industrial Pt/C (cathode) and industrial Pt/C (anode) catalysts were tested. Figure 6a,b is polarization and power density curves of the DMFCs obtained with O₂ as cathodic

gas feed and methanol (2–12 m) as anodic fuel feed in 6 m KOH electrolyte at 80 °C. As shown in Figure 6a–c, the open-circuit voltage (OCV) and peak power density (PPD) on PdAuBiTe are much higher than those on Pt/C at each methanol concentration (Table S3, Supporting Information). In 10 m CH₃OH, the OCV/PPD on PdAuBiTe is 0.974 V/235.7 mW cm⁻². In contrast, the OCV/PPD on Pt/C is only 0.858 V/101.55 mW cm⁻². To the best of our knowledge, the PPD value of PdAuBiTe is the highest reported so far, which is 2.32 times that on Pt/C, 2.16 times that on recently reported Pd–Te nanosheets (109 mW cm⁻²)^[28] and 2.63 times that on core–shell Au@Pd nanoparticles (89.7 mW cm⁻²).^[44] The activity durability test was carried out using a constant current method at 200 mA cm⁻². The PdAuBiTe ANSs exhibit much higher durability than that of Pt/C throughout the test (Figure 6d). After 54 000 s, the cell voltage on Pt/C decayed from 0.492 to 0.221 V, a 55.1% drop; while that on PdAuBiTe ANSs decayed from 0.587 to

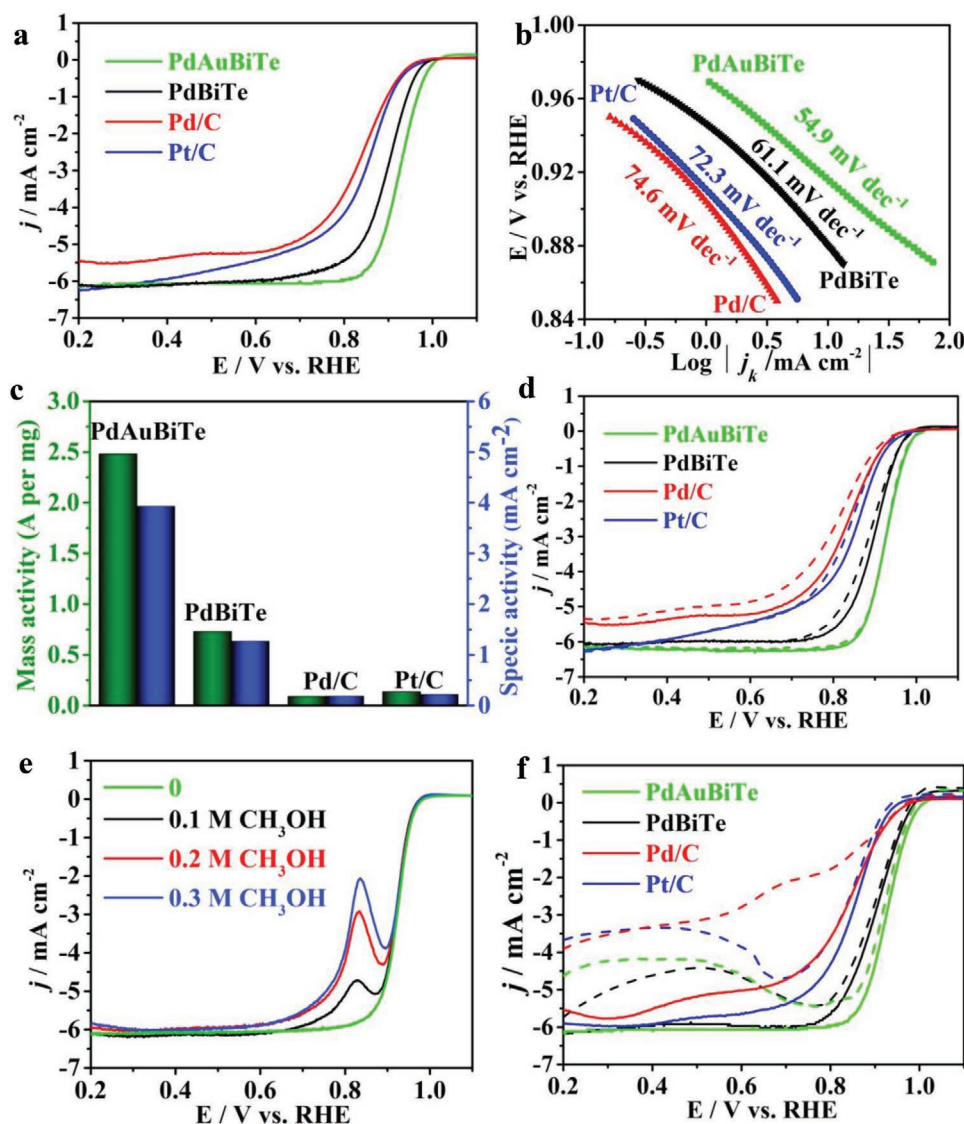


Figure 5. ORR performance of PdAuBiTe, PdBiTe, commercial Pt/C and Pd/C. a) ORR polarization curves, b) Tafel plots, c) histograms of ORR SA and MA recorded at 0.9 V, d) durability test (The solid line represents the ORR polarization curves before ADT, and the dotted line represents after 10 000 potential cycles). e) The response of PdAuBiTe at different CH₃OH concentrations in O₂-saturated 0.1 M KOH. f) The comparisons of the in situ CO ORR polarization curves of PdAuBiTe, PdBiTe, commercial Pd/C and Pt/C with a flow rate of 10 mL min⁻¹ (the solid line represents the ORR polarization curves without CO, and the dotted line represents in the presence of CO).

0.499 V, only a 15.0% drop. Furthermore, the maximum PPD on PdAuBiTe obtained at 60/70 °C is 134.7/190.3 mW cm⁻² (Figure S14, Supporting Information), while that on Pt/C is 54.9/93.7 mW cm⁻² (Figure S14, Supporting Information), further revealing that PdAuBiTe ANSs have much better performance for practical DMFCs. Considering the cost and safety of O₂, we investigated the performance test at 80 °C with much cheaper air as the cathodic gas feed. Figure 6e displayed that a maximum PPD of 173.5 mW cm⁻² with a current density of 500 mA cm⁻² could be achieved on PdAuBiTe ANSs, and the maximum PPD on Pt/C was 48.3 mW cm⁻² with a current density of 111 mA cm⁻². The PPD on Pt/C went down by 52.4% relative to the PPD in O₂, while that on PdAuBiTe ANSs went down only by 26.4%, showing that PdAuBiTe ANSs is less

affected by the concentration of O₂ due to much faster ORR kinetics than Pt/C. The maximum PPD on PdAuBiTe ANSs is 3.59 times that on Pt/C in air. Simultaneously, at 200 mA cm⁻², the PdAuBiTe ANSs exhibited excellent activity durability in the air. After 72 000 s of continuous testing, the cell voltage decayed by only 15.9% from its initial value (Figure 6f). And the stability decline would be caused by electrochemical dealloying process, which was confirmed by XPS analysis. The XPS (Figure S15, Supporting Information) showed that the part of Te was oxidized or dissolved and Bi was dissolved in the PdAuBiTe ANSs. The above performance tests indicated that the prepared PdAuBiTe ANSs can be used as a promising cathode electrocatalyst instead of Pt in actual alkaline DMFCs, especially with air as cathodic gas feed.

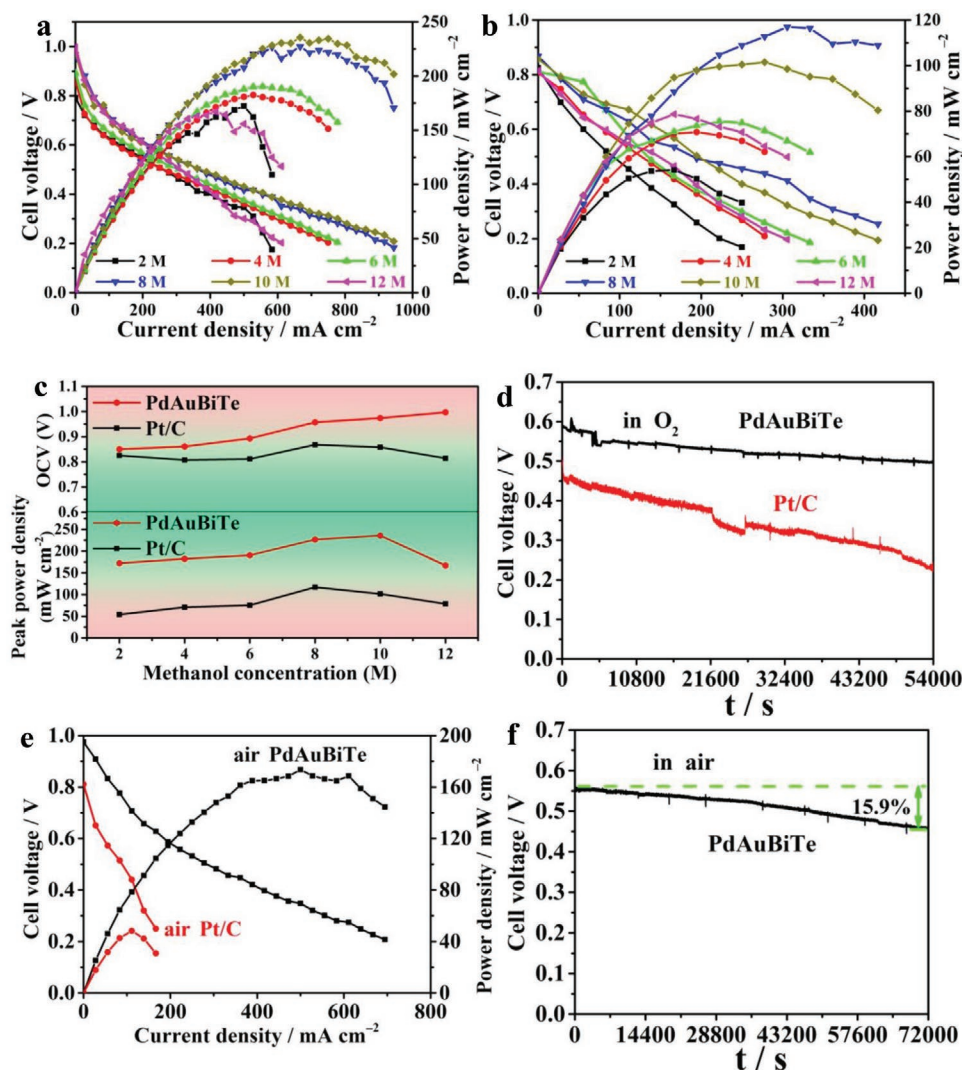


Figure 6. Electrocatalytic performance of PdAuBiTe and commercial Pt/C for practical alkaline DMFCs. a,b) Polarization and power density curves with PdAuBiTe (a) and commercial Pt/C (b) as the cathode in 6 M KOH containing different methanol concentrations. c) Line chart of OCV (top) and PPD (bottom) with different concentration CH_3OH with PdAuBiTe and Pt/C as the cathode. d) Durability test of PdAuBiTe or Pt/C for 54 000 s at 200 mA cm^{-2} in a pure oxygen atmosphere. e) Power density and polarization curves of PdAuBiTe or Pt/C, and f) durability test of PdAuBiTe in air in 6 M KOH + 10 M CH_3OH for 72 000 s at 200 mA cm^{-2} .

3. Conclusion

Ultrathin 2D quaternary PdAuBiTe alloyed nanosheets have been successfully manufactured by a using visible-light-induced template method in an ambient environment. This method can be extended further to prepare ultrathin 2D ternary PdBiTe and AuBiTe alloyed nanosheets. The thickness of as-prepared nanosheets is about 5 nm with diameters larger than 500 nm. The horizontal to vertical ratio exceed 100. The integration of topmost and edge defects, low-coordinated atoms, lattice strain, d-band center downshifting of Pd, and the ensemble effects imparted the PdAuBiTe ANSs much higher ORR performances with high methanol tolerance and antipoisoning to CO than the commercial Pd/C and Pt/C. Control experiments showed that the Au plays a key role in the enhanced ORR performance. The ORR MA of the PdAuBiTe ANSs at 0.9 V (vs RHE) can boost

to 2.48 $\text{A mg}_{\text{Pd}}^{-1}$, which is 27.5 or 17.7 times that of Pd/C or Pt/C, respectively. In the practical DMFCs, at an operating temperature of 80 °C, the maximum power densities of PdAuBiTe ANSs are 235.7/173.5 mW cm^{-2} in O_2/air , respectively, while that on Pt/C are 101.5/48.3 mW cm^{-2} in O_2/air . Simultaneously, the PdAuBiTe ANSs exhibited higher long-term durability in DMFCs measurements. This work not only develops an effective strategy for the preparation of ultrathin 2D multimetallic nanosheets and adds new members to the 2D metal nanostructure family, but also provides a high-performance non-platinum ORR electrocatalyst for practical DMFCs.

Supporting Information

Supporting Information is available from the Wiley Online Library or from the author.

Acknowledgements

This work was supported by the National Natural Science Foundation of China (21571038, 22035004), the National Key R&D Program of China (2017YFA0700101), Foundation of Guizhou Province (2019-5666) and Education Department of Guizhou Province (2021312), State Key Laboratory of Physical Chemistry of Solid Surfaces (Xiamen University, 202009), and the Open Fund of the Key Lab of Organic Optoelectronics & Molecular Engineering (Tsinghua University).

Conflict of Interest

The authors declare no conflict of interest.

Author Contributions

Q.Y. and X.W. conceived, planned, and designed the experiments. Q.Y., S.Y., Z.Z., L.G., and X.W. supervised the work. F.Z. synthesized materials and performed the ORR measurements. F.Z., X.Y., and Z.Z. performed the methanol fuel cells measurements. F.Z., X.Y., Q.Z., H.X., Y.G., and L.G. carried out morphology and structure characterizations. L.Z. performed XAFS measurements and analyzed data. Q.Y., F.Z., and X.W. wrote the manuscript.

Data Availability Statement

Research data are not shared.

Keywords

2D nanostructures, direct methanol fuel cell devices, oxygen reduction reaction, Pd-based nanoalloys, ultrathin nanosheets

Received: May 4, 2021

Revised: June 10, 2021

Published online: August 31, 2021

- [1] A. C. Chen, C. Ostrom, *Chem. Rev.* **2015**, *115*, 11999.
- [2] N. Kakati, J. Maiti, S. H. Lee, S. H. Jee, B. Viswanathan, Y. S. Yoon, *Chem. Rev.* **2014**, *114*, 12397.
- [3] F. Xiao, Y. C. Wang, Z. P. Wu, G. Y. Chen, F. Yang, S. Q. Zhu, K. Siddharth, Z. J. Kong, A. L. Lu, J. C. Li, C. J. Zhong, Z. Y. Zhou, M. H. Shao, *Adv. Mater.* **2021**, 2006292.
- [4] E. Antolini, *Energy Environ. Sci.* **2009**, *2*, 915.
- [5] X. X. Wang, M. T. Swihart, G. Wu, *Nat. Catal.* **2019**, *2*, 578.
- [6] D. Wang, S. Liu, J. Wang, R. Lin, M. Kawasaki, E. Rus, K. E. Silberstein, M. A. Lowe, F. Lin, D. Nordlund, H. Liu, D. A. Muller, H. L. Xin, H. D. Abruña, *Nat. Commun.* **2016**, *7*, 11941.
- [7] C. Koenigsmann, S. S. Wong, *ACS Catal.* **2013**, *3*, 2031.
- [8] J. Li, H. Yin, X. Li, E. Okunishi, Y. Shen, J. He, Z. Tang, W. Wang, E. Yücelen, C. Li, Y. Gong, L. Gu, S. Miao, L. Liu, J. Luo, Y. Ding, *Nat. Energy* **2017**, *2*, 17111.
- [9] X. Tian, X. Zhao, Y. Su, L. Wang, H. Wang, D. Dang, B. Chi, H. Liu, E. J. M. Hensen, X. W. Lou, B. Y. Xia, *Science* **2019**, *366*, 850.
- [10] M. A. Z. Gul Sial, M. A. Ud Din, X. Wang, *Chem. Soc. Rev.* **2018**, *47*, 6175.
- [11] L. Wang, Z. H. Zeng, W. P. Gao, T. Maxson, D. Raciti, M. Giroux, X. Q. Pan, C. Wang, J. Greeley, *Science* **2019**, *363*, 870.
- [12] C. L. Tan, X. H. Cao, X. J. Wu, Q. Y. He, J. Yang, X. Zhang, J. Z. Chen, *Chem. Rev.* **2017**, *117*, 6225.
- [13] W. J. Zhu, L. Zhang, P. P. Yang, C. L. Hu, Z. B. Luo, X. X. Chang, Z. J. Zhao, J. L. Gong, *Angew. Chem., Int. Ed.* **2018**, *57*, 11544.
- [14] M. Zhou, C. Li, J. Fang, *Chem. Rev.* **2021**, *121*, 736.
- [15] M. A. Ud Din, F. Saleem, B. Ni, Y. Yong, X. Wang, *Adv. Mater.* **2017**, *29*, 1604994.
- [16] Y. P. Zuo, D. W. Rao, S. Li, T. T. Li, G. L. Zhu, S. M. Chen, L. Song, Y. Chai, H. Han, *Adv. Mater.* **2018**, *30*, 1704171.
- [17] L. Chong, J. Wen, J. Kubal, F. G. Sen, J. Zou, J. Greeley, M. Chan, H. Barkholtz, W. Ding, D. J. Liu, *Science* **2018**, *362*, 1276.
- [18] Z. Y. Liu, Z. P. Zhao, B. S. Peng, X. F. Duan, Y. Huang, *J. Am. Chem. Soc.* **2020**, *142*, 17812.
- [19] C. Li, Q. Yuan, B. Ni, T. He, S. Zhang, Y. Long, L. Gu, X. Wang, *Nat. Commun.* **2018**, *9*, 3702.
- [20] P. Strasser, S. Koh, T. Anniyev, J. Greeley, K. More, C. Yu, Z. Liu, S. Kaya, D. Nordlund, H. Ogasawara, M. F. Toney, A. Nilsson, *Nat. Chem.* **2010**, *2*, 454.
- [21] S. Chen, J. K. Zhao, H. Y. Su, H. L. Li, H. L. Wang, Z. P. Hu, J. Bao, J. Zeng, *J. Am. Chem. Soc.* **2021**, *143*, 496.
- [22] X. Huang, S. Tang, X. Mu, Y. Dai, G. Chen, Z. Zhou, F. Ruan, Z. Yang, N. Zheng, *Nat. Nanotechnol.* **2011**, *6*, 28.
- [23] G. Wu, X. S. Zheng, P. X. Cui, H. Y. Jiang, X. Q. Wang, Y. T. Qu, W. X. Chen, Y. Lin, H. Li, X. Han, Y. M. Hu, P. G. Liu, Q. H. Zhang, J. J. Ge, Y. C. Yao, R. B. Sun, Y. Wu, L. Gu, X. Hong, Y. D. Li, *Nat. Commun.* **2019**, *10*, 4855.
- [24] H. Xu, H. Shang, C. Wang, Y. K. Du, *Small* **2021**, *17*, 2005092.
- [25] J. W. Hong, Y. Kim, D. H. Wi, S. Lee, S. U. Lee, Y. W. Lee, S. I. Choi, S. W. Han, *Angew. Chem., Int. Ed.* **2016**, *55*, 2753.
- [26] S. P. Luo, W. Chen, Y. Cheng, X. Song, Q. L. Wu, L. X. Li, X. T. Wu, T. H. Wu, M. R. Li, Q. Yang, K. R. Deng, Z. W. Quan, *Adv. Mater.* **2019**, *31*, 1903683.
- [27] M. Luo, Z. Zhao, Y. Zhang, Y. Sun, Y. Xing, F. Lv, Y. Yang, X. Zhang, S. Hwang, Y. Qin, J. Y. Ma, F. Lin, D. Su, G. Lu, S. Guo, *Nature* **2019**, *574*, 81.
- [28] Y. Zhang, B. L. Huang, G. Luo, T. Sun, Y. G. Feng, Y. C. Wang, Y. H. Ma, Q. Shao, Y. F. Li, Z. Y. Zhou, X. Q. Huang, *Sci. Adv.* **2020**, *6*, eaba9731.
- [29] L. Bu, N. Zhang, S. Guo, X. Zhang, J. Li, J. Yao, T. Wu, G. Lu, J. Y. Ma, D. Su, X. Huang, *Science* **2016**, *354*, 1410.
- [30] H. Y. Su, Y. Gorlin, I. C. Man, F. Calle-Vallejo, J. K. Nørskov, T. F. Jaramillo, J. Rossmeisl, *Phys. Chem. Chem. Phys.* **2012**, *14*, 14010.
- [31] J. C. Dong, X. G. Zhang, V. Briega-Martos, X. Jin, J. Yang, S. Chen, Z. L. Yang, D. Y. Wu, J. M. Feliu, C. T. Williams, Z. Q. Tian, J. F. Li, *Nat. Energy* **2019**, *4*, 60.
- [32] X. L. Tian, X. F. Lu, B. Y. Xia, X. W. Lou, *Joule* **2020**, *4*, 45.
- [33] Z. W. Seh, J. Kibsgaard, C. F. Dickens, I. Chorkendorff, J. K. Nørskov, T. F. Jaramillo, *Science* **2017**, *355*, eaad4998.
- [34] V. Vij, S. Sultan, A. M. Harzandi, A. Meena, J. N. Tiwari, W. Lee, T. Yoon, K. S. Kim, *ACS Catal.* **2017**, *7*, 7196.
- [35] Z. Ma, Z. P. Cano, A. P. Yu, Z. W. Chen, G. P. Jiang, X. G. Fu, L. Yang, T. P. Wu, Z. Y. Bai, J. Lu, *Angew. Chem., Int. Ed.* **2020**, *59*, 18334.
- [36] Y. Wang, Y. Yang, S. F. Jia, X. M. Wang, K. Lyu, Y. Q. Peng, H. Zheng, X. Wei, H. Ren, L. Xiao, J. B. Wang, D. A. Muller, H. D. Abruña, B. J. Hwang, J. T. Lu, L. Zhuang, *Nat. Commun.* **2019**, *10*, 1506.
- [37] Y. Yang, W. P. Xiao, X. R. Feng, Y. Xiong, M. X. Gong, T. Shen, Y. Lu, H. D. Abruña, D. L. Wang, *ACS Nano* **2019**, *13*, 5968.
- [38] Y. Yang, G. Chen, R. Zeng, A. M. Villarino, F. J. DiSalvo, R. B. van Dover, H. D. Abruña, *J. Am. Chem. Soc.* **2020**, *142*, 3980.
- [39] J. A. Z. Zeledón, M. B. Stevens, G. T. K. K. Gunasooriya, A. Gallo, A. T. Landers, M. E. Kreider, C. Hahn, J. K. Nørskov, T. F. Jaramillo, *Nat. Commun.* **2021**, *12*, 620.

- [40] D. Sun, Y. F. Wang, K. J. T. Livi, C. H. Wang, R. C. Luo, Z. Q. Zhang, H. Alghamdi, C. Y. Li, F. F. An, B. Gaskey, T. Mueller, A. S. Hall, *ACS Nano* **2019**, *13*, 10818.
- [41] W. L. Jiao, C. Chen, W. B. You, X. R. Zhao, J. Zhang, Y. Z. Feng, P. Wang, R. C. Che, *Adv. Energy Mater.* **2020**, *10*, 1904072.
- [42] R. Chattot, O. L. Bacq, V. Beermann, S. Kühl, J. Herranz, S. Henning, L. Kühn, T. Asset, L. Guétaz, G. Renou, J. Drnec, P. Bordet, A. Pasturel, A. Eychmüller, T. J. Schmidt, P. Strasser, L. Dubau, F. Maillard, *Nat. Mater.* **2018**, *17*, 827.
- [43] K. A. Kuttiyel, K. Sasaki, D. Su, L. Wu, Y. Zhu, R. R. Adzic, *Nat. Commun.* **2014**, *5*, 5185.
- [44] Y. Feng, H. Liu, J. Yang, *Sci. Adv.* **2017**, *3*, e1700580.
- [45] J. I. Langford, D. Lou, *Rep. Prog. Phys.* **1996**, *59*, 131.
- [46] J. R. Kitchin, J. K. Nørskov, M. A. Barteau, J. G. Chen, *Phys. Rev. Lett.* **2004**, *93*, 156801.
- [47] T. Chao, X. Luo, W. X. Chen, B. Jiang, J. J. Ge, Y. Lin, G. Wu, X. Q. Wang, Y. M. Hu, Z. B. Zhuang, Y. E. Wu, X. Hong, Y. D. Li, *Angew. Chem., Int. Ed.* **2017**, *56*, 16047.
- [48] X. J. Zhu, Q. S. Guo, Y. F. Sun, S. J. Chen, J. Q. Wang, M. M. Wu, W. Z. Fu, Y. Q. Tang, X. Z. Duan, D. Chen, Y. Wan, *Nat. Commun.* **2019**, *10*, 1428.
- [49] F. Liu, D. Wechsler, P. Zhang, *Chem. Phys. Lett.* **2008**, *461*, 254.
- [50] V. Stamenkovic, B. S. Mun, K. J. J. Mayrhofer, P. N. Ross, N. M. Markovic, J. Rossmeisl, J. Greeley, J. K. Nørskov, *Angew. Chem., Int. Ed.* **2006**, *45*, 2897.
- [51] A. A. Phatak, W. N. Delgass, F. H. Ribeiro, W. F. Schneider, *J. Phys. Chem. C* **2009**, *113*, 7269.
- [52] K. Sasaki, H. Naohara, Y. Choi, Y. Cai, W. F. Chen, P. Liu, R. R. Adzic, *Nat. Commun.* **2012**, *3*, 1115.
- [53] N. Lopez, J. K. Nørskov, *J. Am. Chem. Soc.* **2002**, *124*, 11262.
- [54] J. Zhang, K. Sasaki, E. Sutter, R. R. Adzic, *Science* **2007**, *315*, 220.
- [55] B. A. Lu, T. Sheng, N. Tian, Z. C. Zhang, C. Xiao, Z. M. Cao, H. B. Ma, Z. Y. Zhou, S. G. Sun, *Nano Energy* **2017**, *33*, 65.
- [56] M. Núñez, J. L. Lansford, D. G. Vlachos, *Nat. Chem.* **2019**, *11*, 449.